REPORT DOCUMENTATION PAGE

Form Approved
OMB No. 0704-0188

PLEASE DO NOT RETURN YOUR FORM TO THE ABOVE ORGANIZATION.

1. REPORT DATE *(DD-MM-YYYY)*	2. REPORT TYPE	3. DATES COVERED *(From - To)*
04-19-2017	Conference paper	1 Jan 2012 - 1 Mar 2013

4. TITLE AND SUBTITLE
APPLICATION OF AN LRF FOR SO IMAGING AND SHAPE RECONSTRUCTION

5a. CONTRACT NUMBER
N/A

5b. GRANT NUMBER
N/A

5c. PROGRAM ELEMENT NUMBER
N/A

6. AUTHOR(S)
Nayak, Michael
Udrea, Bogdan
Marsella, Brandon
Beck, Jaclyn

5d. PROJECT NUMBER
N/A

5e. TASK NUMBER
N/A

5f. WORK UNIT NUMBER
N/A

7. PERFORMING ORGANIZATION NAME(S) AND ADDRESS(ES)
Space Development and Test Directorate, 3548 Aberdeen Ave SE, Albuquerque NM 87117
Embry-Riddle Aeronautical University, 600 S Clyde Morris Blvd, Daytona Beach FL 32114
NASA Goddard Space Flight Center, 8800 Greenbelt Rd, Greenbelt MD 20770

8. PERFORMING ORGANIZATION REPORT NUMBER
N/A

9. SPONSORING/MONITORING AGENCY NAME(S) AND ADDRESS(ES)
Space Development and Test Directorate, 3548 Aberdeen Ave SE, Albuquerque NM 87117

10. SPONSOR/MONITOR'S ACRONYM(S)
SMC/SD

11. SPONSOR/MONITOR'S REPORT NUMBER(S)
N/A

12. DISTRIBUTION/AVAILABILITY STATEMENT
Distribution A. Approved for public release: distribution unlimited.

13. SUPPLEMENTARY NOTES
23rd AAS/AIAA Space Flight Mechanics Meeting, Kauai, Hawaii, February 10-14, 2013

14. ABSTRACT
This paper addresses the feasibility of using point clouds generated with a single-beam laser rangefinder (LRF) to reconstruct the three-dimensional shape of an unknown Resident Space Object (RSO), employing a combination of relative motion between the chaser and the RSO and chaser attitude motion. The first step in the analysis is the application of both an LRF and a scanning LIDAR to image and reconstruct the shape of a tri-axial ellipsoid of diffuse constant reflectivity. A single beam LRF, and a multi-beam scanning LIDAR are simulated. Next, the techniques designed above are applied to the imaging of a Resident Space Object (RSO) in the shape of generic telecommunications satellite. Various inclination and attitude maneuver test cases are explored to obtain a desired level of LRF point cloud density. The study concludes that, for error-free measurements, the LRF can effectively create sufficiently dense point clouds for various asteroid and satellite shaped SOs, with low propellant consumption, by exploiting a designed combination of Keplerian and attitude motion. Finally, the technique is further tested through inclusion of two sensor error models.

15. SUBJECT TERMS
Nanosatellite, laser rangefinder, AFOSR, USAF, object imaging, shape reconstruction, space-based, ISR, space situational awareness

16. SECURITY CLASSIFICATION OF:			17. LIMITATION OF ABSTRACT	18. NUMBER OF PAGES	19a. NAME OF RESPONSIBLE PERSON
a. REPORT	b. ABSTRACT	c. THIS PAGE			MICHAEL NAYAK
UU	UU	UU	NONE	21	19b. TELEPHONE NUMBER *(Include area code)* 808-891-7727

Reset

AAS 13-429

APPLICATION OF A LASER RANGEFINDER FOR SPACE OBJECT IMAGING AND SHAPE RECONSTRUCTION

Michael V. Nayak,[*] Bogdan Udrea,[†] Brandon Marsella[‡] and Jaclyn R. Beck[§]

This paper addresses the feasibility of using point clouds generated with a single-beam laser rangefinder (LRF) to reconstruct the three-dimensional shape of an unknown Resident Space Object (RSO), employing a combination of relative motion between the chaser and the RSO and chaser attitude motion. The first step in the analysis is the application of both an LRF and a scanning LIDAR to image and reconstruct the shape of a tri-axial ellipsoid of diffuse constant reflectivity. A single beam LRF, and a multi-beam scanning LIDAR are simulated. Next, the techniques designed above are applied to the imaging of a Resident Space Object (RSO) in the shape of generic telecommunications satellite. Various inclination and attitude maneuver test cases are explored to obtain a desired level of LRF point cloud density. The study concludes that, for error-free measurements, the LRF can effectively create sufficiently dense point clouds for various asteroid and satellite shaped SOs, with low propellant consumption, by exploiting a designed combination of Keplerian and attitude motion. Finally, the technique is further tested through inclusion of two sensor error models. Results will be applied to ARAPAIMA, a nanosatellite mission funded under the US Air Force Office of Scientific Research University Nanosat Program UNP) Cycle 8.

INTRODUCTION

Orbiting space debris has become a problem of increasing concern, especially in Low Earth Orbit (LEO). A relevant example is the large uncontrolled satellite Envisat and upper stages of launchers of Soviet vintage. Three-dimensional imaging and attitude characterization of such tumbling space debris can open doors to missions aimed at clearing out some of the larger and most dangerous objects in LEO. The imaging can also be used to identify other space materials that are causing problems or are of interest to researchers. In addition, several Space Situational Awareness (SSA) missions rely on the three dimensional (3D) imaging of a Resident Space Object (RSO) for proximity operations, rendezvous or docking applications.

The **A**pplication for **R**SO **A**utomated **P**roximity **A**nalysis and **IMA**ging (ARAPAIMA) mission is a proximity operations mission sponsored by the US Air Force Office of Scientific Re-

[*] Satellite Flight Test Engineer, Research, Development, Test and Evaluation Support Center (RSC), Space Development and Test Directorate, 3548 Aberdeen Ave SE, Albuquerque NM 87117. michael.nayak@kirtland.af.mil.
[†] Assistant Professor, Department of Aerospace Engineering, Embry-Riddle Aeronautical University, 600 S. Clyde Morris Blvd., Daytona Beach, FL 32114.
[‡] MS Candidate, Department of Aerospace Engineering, Embry-Riddle Aeronautical University, 600 S. Clyde Morris Blvd., Daytona Beach, FL 32114.
[§] Computer Scientist, Applied Energy and Technology Directorate, NASA Goddard Space Flight Center, 8800 Greenbelt Rd., Greenbelt MD 20770.

search (AFOSR) and the Air Force Research Laboratory (AFRL) UNP Cycle 8. The mission is designed to perform the in-orbit demonstration of autonomous proximity operations and visible, infrared (IR) and three-dimensional imaging of RSOs from a nanosatellite platform. The mission steps are *1*) establish relative orbit around an RSO of interest, *2*) characterize the attitude motion of the RSO, and *3*) prove the capability of the nanosatellite to plan Rendezvous and Proximity Operations (RPO) algorithms to fly with these uncooperative objects with sufficient accuracy and fidelity to achieve a capture/docking level of confidence.

To accomplish these objectives from a nanosatellite platform, the ARAPAIMA mission hosts a very simple payload, comprising of a Wide Field of View (WFOV) IR camera and a laser rangefinder (LRF). This paper investigates the application of an LRF for generation of a point cloud of an RSO whose attitude motion is well-characterized, with sufficient resolution to provide comparable registration and shape reconstruction to an imaging Light Detection and Ranging (LIDAR) sensor. A method that employs a combination of relative motion between the chaser and the RSO and chaser attitude motion to perform 3D RSO imaging is examined here.

Background: LRF and LIDAR historical applications to 3D Imaging

A time-of-flight LRF is a distance measurement device that employs a laser to determine the distance between itself and an object by using the time of flight of a pulsed laser beam. Space mission utility for time-of-flight LRFs are primarily in three dimensional (3D) mapping of celestial bodies. An example is NASA's Near Earth Asteroid Rendezvous (NEAR) mission, which employed an LRF to aid its rendezvous[6] with asteroid 433 Eros in 2000.

Two types of imaging Light Detection and Ranging (LIDAR) sensors have been in use or are currently tested for space missions. The scanning LIDAR employs spinning mirrors to steer a single beam through 3D space and the flash LIDAR uses modulated laser light to illuminate a scene and a photon mixing device (PMD) sensor to detect both the intensity and the amplitude of the laser light reflected by an object and the distance to the object. The Air Force XSS-11 mission used scanning LIDAR 3D imaging to demonstrate operations such as autonomous spacecraft servicing, spacecraft support, diagnostics and maintenance. NASA JPL's Autonomous Landing and Hazard Avoidance (AL-HAT) project uses a flash LIDAR for planetary landing applications. The high resolution and wide field of regard of the scanning and flash LIDARs result in fewer passes needed to reconstruct the 3D shape of the object under surveillance than those needed by an LRF. However, both types of LIDARs are relatively large and power hungry and certainly beyond the budget of a university nanosatellite project. The XSS-11's Rendezvous [scanning] LIDAR Sensor had a range of a few km, a mass of 10kg and consumed 75W7. The DragonEye 3D flash LIDAR space camera proposed as an AL-HAT sensor for some missions has a range of 1.5km, a mass of 3kg, consumes 35W and requires active cooling. In contrast, LRFs offer lower mass and power use and higher reliability. For example, in contrast, NASA's NEAR laser rangefinder, had a range better than 50km, a mass of just 4.9kg and consumed 15W8.Such characteristics make LRFs attractive to agile nanosatellite technology demonstrator missions or cost-constrained SSA missions such as ARAPAIMA.

SENSOR MODELS

With the above applications in mind, this paper addresses the feasibility of using one-dimensional LRF point cloud information to reconstruct the three-dimensional shape of an unknown RSO. The first step in the analysis is the application of both an LRF and a LIDAR to image and reconstruct the shape of a tri-axial ellipsoid of diffuse constant reflectivity. A single beam LRF, a multi-beam LRF and a LIDAR are simulated. This section outlines the various LIDAR,

multi-beam and LRF models utilized for this analysis. During this step measurements from both types of sensor are assumed ideal. Future sections in this paper will outline simulations conducted with errors included in the metrology chain.

The same ray-tracing algorithm is used for all LRF and LIDAR models to determine the intersection points with the RSO facet, and is based on a ray-tracing algorithm. Rays generated at the LIDAR optical center simulate the laser beams. The ray-triangle intersection algorithm* determines the point of intersection between the ray and a model of the scanned object. In order to test different multi-beam LRF configurations, three beam patterns have been implemented: grid, cross, and zigzag. These were chosen due to their commonality on past missions such as the Lunar Observer laser altimeter (LOLA) or future missions.

Setup: Grid Beam Pattern

The LIDAR beam pattern is set up in a rectangular or square pattern similar to that used in the Airborne LIDAR surface Topography (LIST) Simulator.[1].

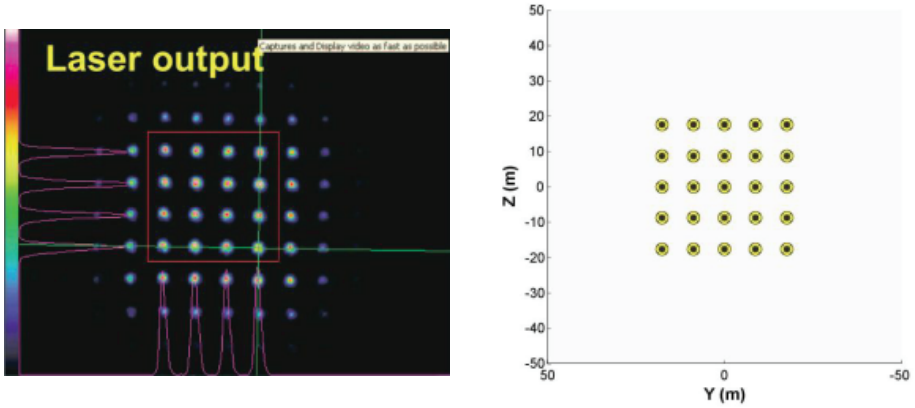

(a) Actual grid pattern LIDAR output[1]

(b) Resolution = 5×5
Azimuth x elevation FoV = $20^{o}\times20^{o}$

Figure 1. Grid pattern: Output of an actual and simulated imaging LIDAR.

The resolution is defined as the total number of strike points that the grid will contain. The pattern is defined by both an azimuth and an elevation resolution, as well as the field of view (FOV) azimuth and elevation angle. Different angles can be defined for the field of view parameters on each side of the optical axis, as seen in Figure 2.

* The algorithm is available on the MATLAB Central File Exchange at http://www.mathworks.us/matlabcentral/fileexchange/33073-triangleray-intersection

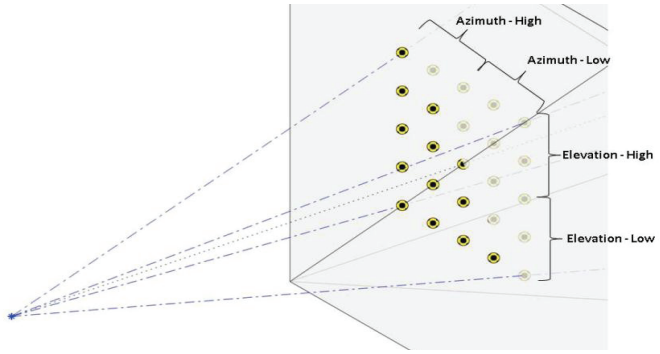

Figure 2. FOV Definition: Optical axis of scanning LIDAR (Black dotted line).

Adjusting these angles will result in a slightly offset or skewed grid, shown in Figure 3(b).

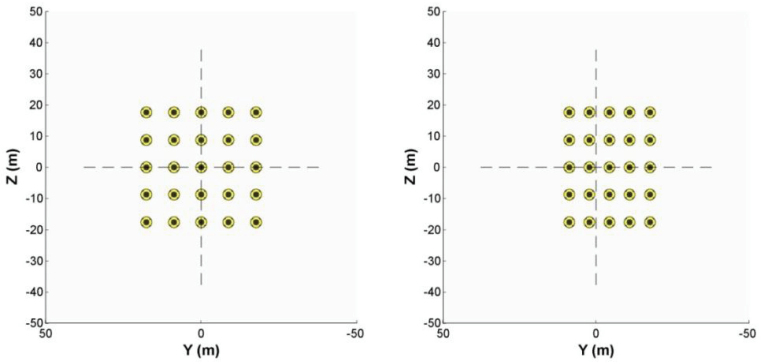

(a) Resolution = 5×5
Azimuth × elevation FoV = 20°×20°

(b) Resolution = 5×5
Azimuth × elevation FoV = 15°×20°

Figure 3. Grid Results from LIDAR algorithm. Both images have the same pointing axis; the only change is to the FOV definition.

Cross Beam Pattern

The cross-beam LRF pattern is similar to the configuration implemented on the LOLA as seen in Figure 4(a).[2] This configuration is defined as a five beam LRF, where the center beam is aligned along the main pointing axis and the other four beams are along the FOV extremes. This setup is shown in Figure 4(b).

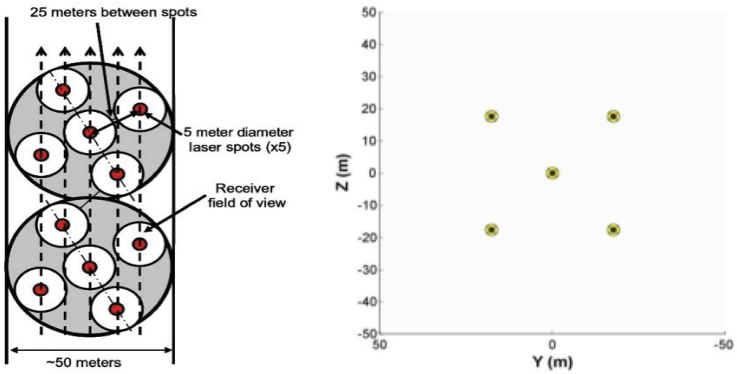

(a) Actual LOLA grid pattern LRF output[2] (b) Results from cross LRF set up Azimuth × Elevation: 20°×20°.

Figure 4: LOLA cross LRF pattern and the simulated cross LRF model

Zigzag Beam Pattern

The zigzag multi-beam LRF is similar to that used in the NASA LIDAR Surface Topography (LIST) proposed space flight mission. In this mission the instrument generates a 1000 beam pattern in a 5km strip as seen in Figure 5(a).[2] The FOV is defined as in the previous two LRF configurations. The setup is mainly defined by the number of beams, which specifies the beams in each offset pattern. These beams are then equally spaced through the elevation parameter with two offset rows, one at the higher elevation and one at the lower elevation FOV parameter, as shown in Figure 5(b).

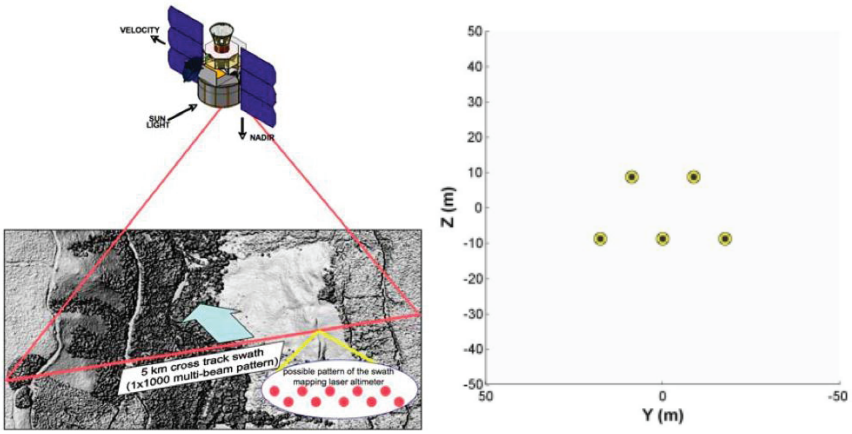

(a) Actual zigzag pattern LIDAR output[2] (b) Results from zigzag LIDAR algorithm: Errors off, Az×El: 20°×10°, Beams = 5

Figure 5: Proposed LIST zigzag and the simulated imaging LRF zigzag model.

CASE STUDY: GENERIC TRI-AXIAL ELLIPSOID

The study of a generic tri-axial ellipsoid is undertaken with the above sensor models described above. The LRFs leverage an orbit that combines Keplerian motion with a scanning attitude mo-

tion, as opposed to a nadir-pointing attitude profile. The LIDAR flies in a nadir-pointing orbit, i.e., with the optical axis of its receiver pointing at the geometric center of the ellipsoid. The resulting measurements from the LRF simulations are compared to the LIDAR simulation results to judge viability for shape reconstruction to the case of 3D imaging of an asteroid-like body.

Model: Tri-Axial Ellipsoid and Keplerian Motion

The asteroid is a tri-axial ellipsoid that is Delaunay triangulated. Its axis of rotation is mainly about the z-axis in the inertial reference frame. It has a period of rotation of 15480 seconds, or 4.3 hours. The axes are set to fixed values of 143.75 meters, 86.25 meters, and 287.50 meters along the x-, y-, and z-axis respectively as shown in Figure 6.

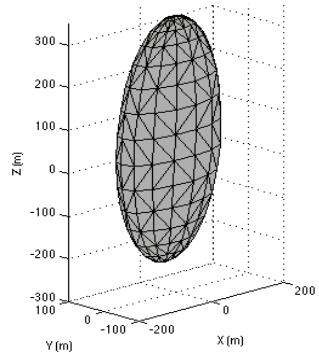

Figure 6: Asteroid modeled as a tri-axial ellipsoid.

The radius of the spacecraft orbit is set to 750 meters and propagated using Keplerian motion. The spacecraft is incrementally moved along the orbit path in time steps of 10 seconds. An LRF strike is simulated by using the nadir vector as the beam path and calculating the intersections with the beam and the triangles that make up the asteroid. If an intersection is found, its position is recorded as an LRF strike point. The quality of coverage of a point cloud is calculated using an edge metric developed by the authors[4]. The metric calculates how well the triangulation of the ellpsoid is reconstructed from the point cloud. Scores are between 0 and 1, with lower scores indicating lower error and more accurate reconstruction. In general, rough shapes can be reconstructed from point clouds that score below 0.3, although fine detail and small edges may be lost[4].

Results: Single-beam LRF Imaging of a Tri-Axial Ellipsoid

Two initial tests on the asteroid are conducted to determine baseline coverage scores for the LRF, against which future results can be compared. In the first test, simulations are run at several different orbit inclinations relative to the x-y plane to evaluate coverage for a fixed amount of time – in this case 100 rotations of the asteroid (17.92 days). It is found that an inclination between 85 and 90°, measured with reference to the plane of the asteroid, gives the lowest score and best coverage. This is evident from Figure 7(a).

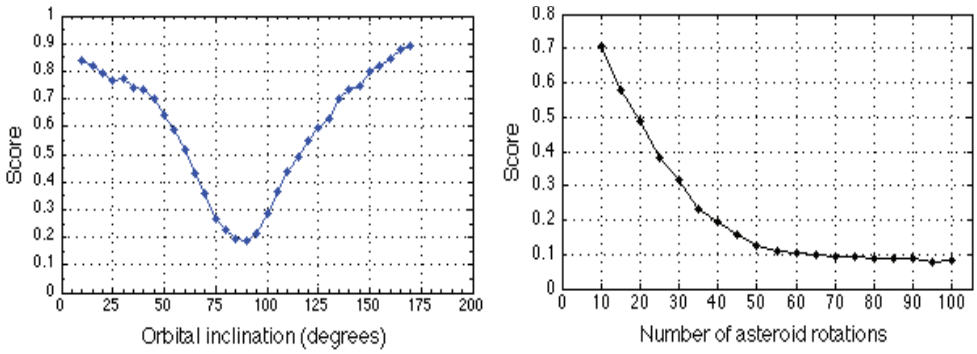

(a) Shape Reconstruction score vs. orbital inclination

(b) Shape Reconstruction score vs. number of asteroid rotations

Figure 7: Baseline Tests: Score vs. asteroid rotations and inclination

In the second test, the spacecraft is allowed to orbit the asteroid for varying amounts of time along an orbit, collecting strike points. The objective of this test was to see how long the spacecraft needed to orbit in order for LRF coverage to approach a reference level of coverage obtained from LIDAR simulations, covered in the next section. The duration of the imaging is simulated as lasting between 10 and 100 asteroid rotations (43 hours to 17.92 days) at a nearly-polar orbit of 85°. Figure 7(a) shows the results of Test 1. The change in coverage score over time levels out between 50 and 60 rotations (8.95 days to 10.75 days), so 50 rotations are used in further trials that require a fixed time.

Further analysis of the results from Test 1 shows that for point clouds generated in a polar orbit, two large gaps manifest themselves as "blind spots" to the LRF. This is shown in Figure 8(b). Allowing the spacecraft to orbit for longer periods of time (100, 150, and 200 rotations) does not fill these gaps. These gaps close in the 85° point cloud (Figure 8(a)), so 85° to be the near-optimal inclination for future asteroid simulations.

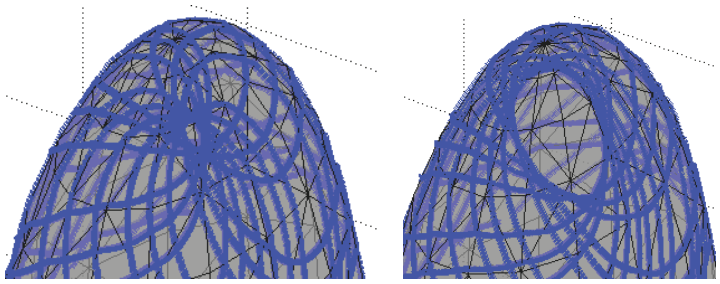

(a) LRF, 85° orbital inclination, 50 asteroid rotations

(b) LRF, 90° orbital inclination, 50 asteroid rotations

Figure 8: LRF Inclination Tests: 85° vs. 90° inclination

It is apparent from the baseline tests, as well as from the coverage obtained in Figure 8 after 50 asteroid rotations (nearly 18 days), that simply allowing the spacecraft to orbit passively will not result in comparable coverage to a LIDAR in an operationally practical amount of time. The advantage of the LIDAR comes from getting data in both the azimuth and elevation in one shot. In the case of single or multi-beam LRF the spacecraft attitude is commanded to perform a scanning motion to fill in the target with strike points. This results in the strike points covering a wider path as the spacecraft moves along its orbit, but it also means that the distance in between each strike point on the asteroid is increased, resulting in lower resolution per pass.

As the ultimate mission goal is RSO shape reconstruction, vs fine-grain mapping, the loss in resolution is considered as an acceptable compromise. To quantify the effects of slewing on LRF coverage, the performance difference is examined between imaging without attitude maneuvers and a attitude maneuvers that perform a slew with an amplitude of 2° from the nadir line, in a place normal to the orbital plane. Figure 9(a) shows the results for both cases, at the near-optimal 85° inclination, between 10 and 100 rotations. While both scores start to level off between 40 and 60 rotations, the scores for slew angle are consistently lower than the scores for no slewing. Further, slewing clearly decreases the amount of time necessary to reconstruct the asteroid's shape with reasonable certainty.

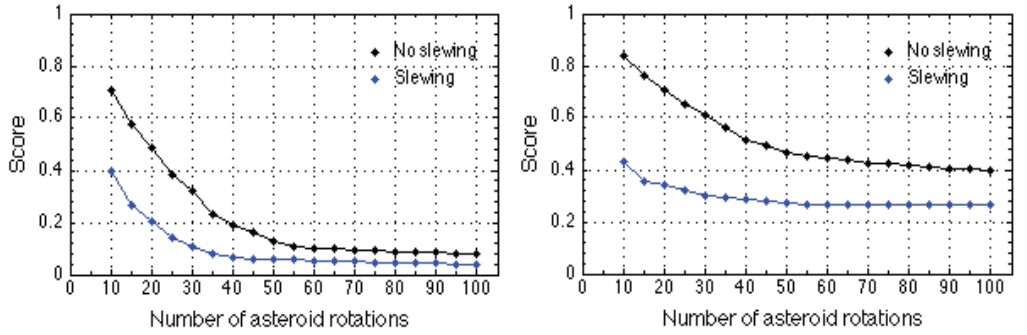

(a) Shape Reconstruction score vs. # of asteroid rotations (85° inclination)

(b) Shape Reconstruction score vs. # of asteroid rotations (70° inclination)

Figure 9: Score vs. asteroid rotations for optimal (left) and suboptimal (right) inclinations

Figure 9(b) shows the results from repeating the previous trials at a suboptimal inclination of 60°, where it is not expected to obtain full coverage of the asteroid. A wider slew angle of 5° in each direction is contrasted against no attitude maneuvers. The difference in scores between the two trials is much more pronounced at a suboptimal inclination; the slew trial scores better at 15 rotations than the non-slewing trial does after 100 rotations. For a realistic, non-optimal asteroid surveillance scenario, this suggests that leveraging slew attitude maneuvers is a way to optimize coverage quickly.

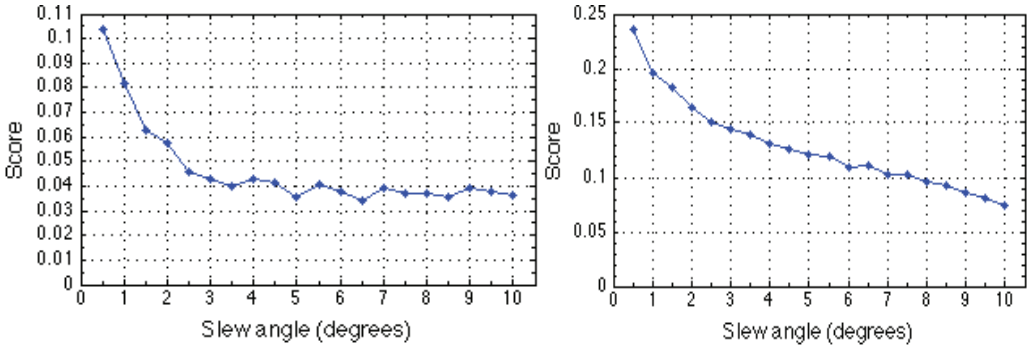

(a) Shape Reconstruction score vs. Slew angle (85° inclination)

(b) Shape Reconstruction score vs. Slew angle (70° inclination)

Figure 10: Score vs. slew angle for optimal (left) and suboptimal (right) inclinations

Figure 10 shows the results of an attempt to determine if shape reconstruction can be improved by varying the slew angle. For the near-optimal inclinations, no significant improvement is noted beyond a slew angle of 3°, with increasing loss of area resolution. At suboptimal inclinations, the score improves steadily as slew angle increases, because the wider angle allows us to compensate for missed coverage at the poles of the asteroid.

Results: Multi-beam LRF Imaging of a Tri-Axial Ellipsoid

For ellipsoid mapping with a multi-beam LRF, the simulation is set up identical to that employed for the LRF tests – a period of rotation of 15480s and an orbital radius of 750m.

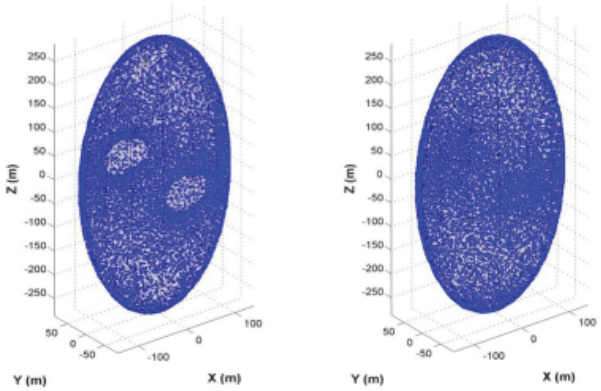

Figure 11: Multi-beam LRF in the cross configuration (left) vs. zigzag configuration (right). The coverage is comparable.

The cross configuration field of view is set to 10°×10°. With this setting a point cloud of 15,674 strikes is generated as seen in Figure 11. The coverage is obviously excellent, yielding an edge metric score of 0.0789. The figure also shows the zigzag configuration, with 16,125 strikes and an edge metric score of 0.0833. The cross configuration yields worse results early in the simulation, though they converge to be closer to the zigzag results after several rotations of the asteroid. Therefore, it is concluded that the two models are practically equivalent.

Finally, the imaging results are brought together to compare the performance of a slewing LRF to that of an imaging LIDAR. In a LIDAR simulation of 15 asteroid rotations at an orbital inclination of 85°, the multi-beam point cloud achieved a score of 0.02. As seen in Figure 12, this score is can be obtained by slewing the LRF beam and allowing the spacecraft to orbit for at least 50 rotations of the asteroid.

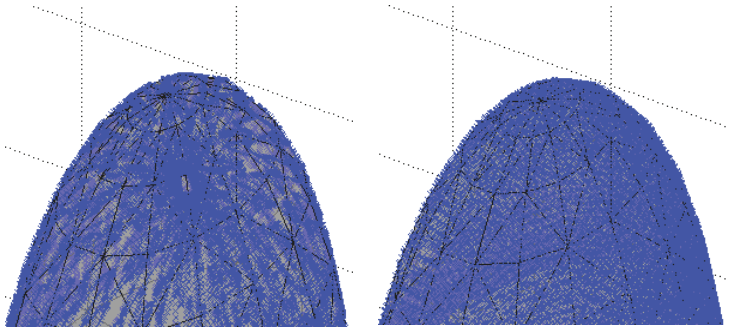

(a) LRF, 85° inclination, 50 asteroid rotations, 2° slew angle, score of 0.058

(b) LIDAR, 85° inclination, 15 asteroid rotations, score of 0.02

Figure 12: Slewing LRF vs. nadir-pointing LRF: Comparable coverage scores

The difference in coverage between Figure 8 and Figure 12 is evident. It is concluded that the coverage obtained is comparable to that of an imaging LIDAR, albeit achieved after a longer duration. This is sufficient fidelity to warrant an investigation into LRF coverage of an RSO for SSA mission purposes, such as those proposed for ARAPAIMA. In addition, the techniques designed above are applicable to the case of creating 3D maps of asteroids and comets.

CASE STUDY: GENERIC RESIDENT SPACE OBJECT

In this section, the techniques designed above are applied to reconstructing a satellite RSO, in the shape of a generic telecommunications satellite, whose attitude information is known, i.e., a stable RSO. Various inclination and attitude maneuver test cases are explored to obtain a desired level of LRF point cloud density and draw conclusions regarding the fidelity of the proposed ARAPAIMA payload.

Model: Satellite-shaped RSO

Two RSO shapes are used for analysis. The first RSO, hereafter referred to as RSO A, has a bus shaped as a cube body, with an edge of 5m, with a sphere and a disk protruding from one of the faces. It has two solar panels that make the RSO oblate along its x-axis. The second, RSO B, has a rectangular body that consists of two stacked cubes. It has two cylindrical protrusions and a long pole with a disk at the end. It is less oblate than RSO A but contains more fine detail. Both RSOs are 20 meters wide along the axis of their solar panels. Figure 13 illustrates both models.

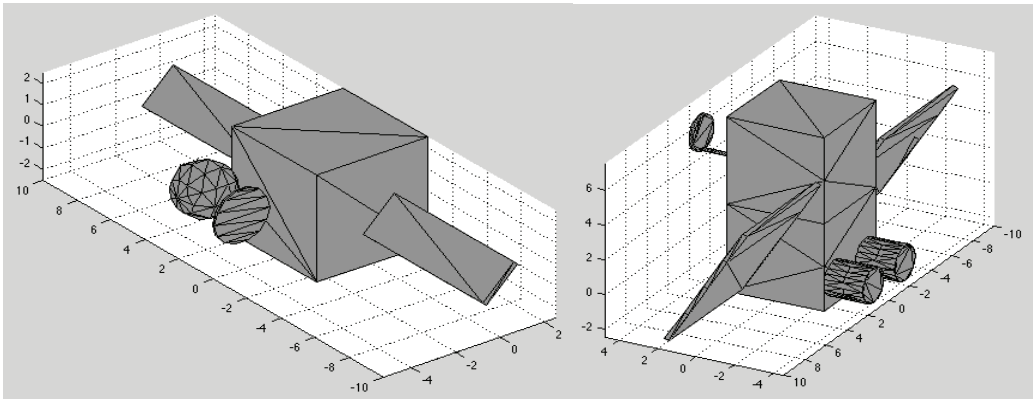

Figure 13: Modeled satellite RSOs: RSO-A (left) and RSO-B (right).

As with the asteroid, the coverage of the RSO is evaluated with the edge metric. However, the edge recognition algorithm used earlier does poorly on solar panels, in part because they generally are not covered well by the points in the cloud, but also because they are thin objects. The algorithm works by measuring changes in surface variance[4] as points in a neighborhood are added or removed, and in a neighborhood where many of the nearest neighbors are on a nearby parallel surface, surface variance will change whenever any point in the neighborhood is added or removed, so all points are likely to be marked as edge points. The sheer amount of false positives on the solar panels is enough to skew metric results. Imaging with a LIDAR is much better than that obtained with an LRF: therefore, the LIDAR score of a shape is used as a baseline; coverage is judged relative to a LIDAR baseline rather than scores as absolutes across all types of shapes.

Results: LRF Imaging of satellite-shaped RSO

The asteroid analysis, presented above, is used to set baseline conditions for the following simulations. The orbit is set up identical to that of the asteroid tests (i.e. period of rotation of 15480s, orbital radius of 250m, and maximum time of 50 RSO rotations or 129 hours). The asteroid is imaged every 10 seconds. To simulate part of the ARAPAIMA Concept of Operations (CONOPS), the closest approach of the spacecraft is set to 250 meters from the RSO. For the purposes of comparison with the asteroid, the RSO tumbles in a controlled manner about its z-axis with a rotational period of 4.3 hours.

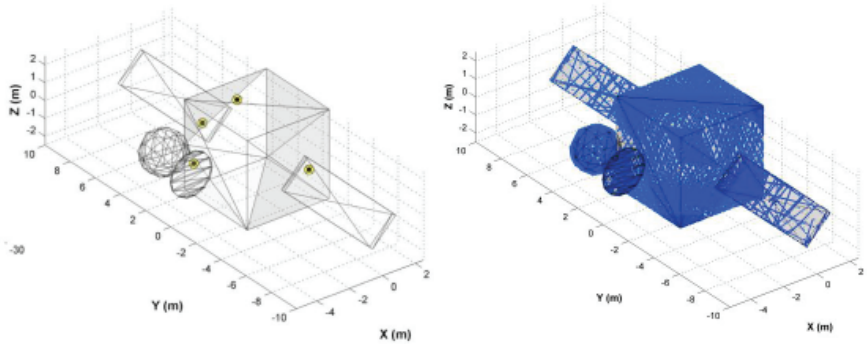

(a) Sample multi-beam zigzag configuration pattern (b) Point Cloud

Figure 14: Results for Cross configuration LRF Imaging of RSO

Due to the small size of the RSO the field of view had to be decreased greatly in order to fully utilize the multi-beam capabilities. The field of view is set to 1.2^{o}x1.2^{o}. With this setting, and a cross-configuration, a point cloud is generated as seen in Figure 14. Note that not all five beams strike the RSO in this image. Running the edge detection metric on the point cloud shown above results in a score of 0.1576 after 129 hours.

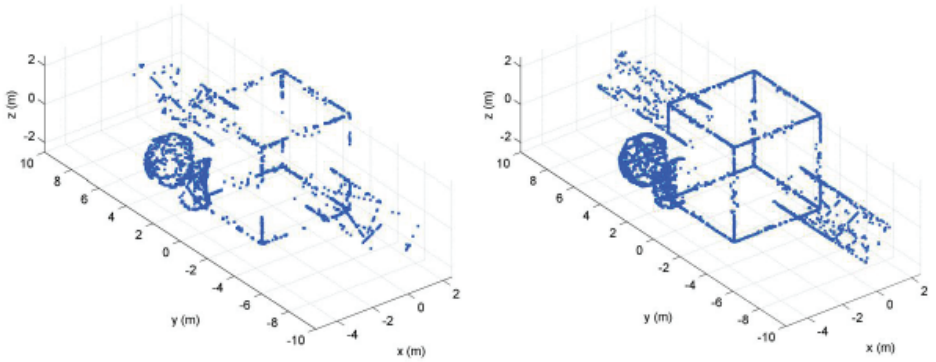

(a) 43 Hours (b) 129 Hours

Figure 15: Edge Detected Points Cross configuration LRF Imaging of RSO

Results: Single-beam LRF Imaging of satellite-shaped RSO

Several of the earlier tests conducted on an asteroid are recreated for the RSO case.

Surveillance time. As before, the spacecraft is set at a relative inclination of 85° and allowed to orbit for a fixed amount of time. As might be expected, it takes much less time to form a recognizable shape for the RSO than the asteroid, as both RSOs are far smaller. After only one RSO rotation (4.3 hours), the edge recognition algorithm can find most of the large edges of each RSO and some of the smaller detail edges. Details are presented in Figure 16 below.

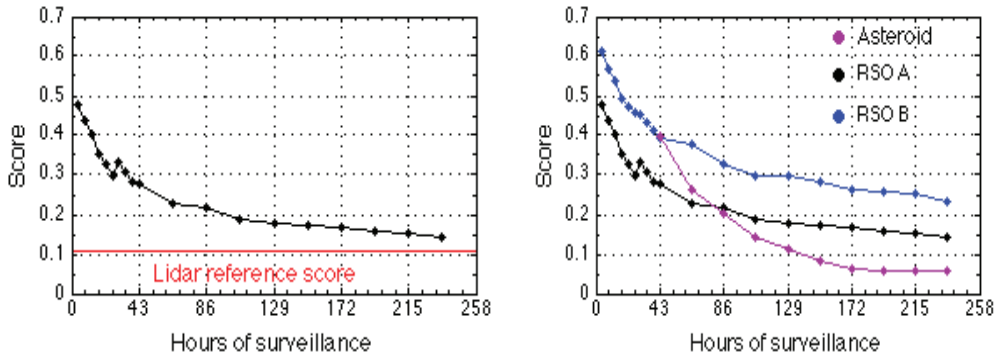

Figure 16: RSO-A Score vs. surveillance time: against the LIDAR reference (left), and against RSO-B and Asteroid scores (right).

Despite the fact that scores appear to be worse for the RSOs, the man-made shape of the RSO, with its many abrupt edges, is easily recognized both with the naked eye and by the edge detection algorithm[4,5] in much less time than with the asteroid. This is evident from Figure 17 below.

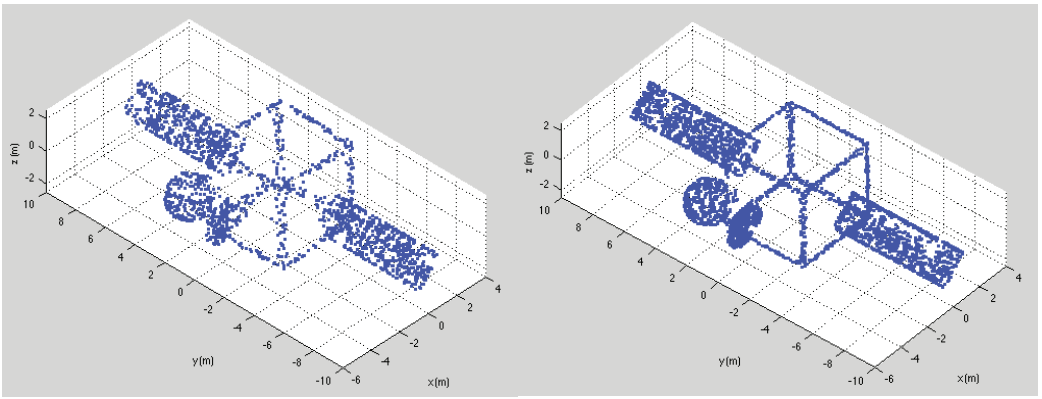

Figure 17: LRF-only surveillance: Edge points found after 43 hours (left) and 129 hours (right).

Axis of slew motion. For RSO surveillance, it is found that Keplerian coverage is dependent upon which axis the slew motion occurs around. Coverage is best if the chaser spacecraft slews the LRF beam along the longest axis of the RSO, ensuring maximum spread of points. For ARAPAIMA mission scenarios, no a priori knowledge of RSO shape is assumed, therefore in an operational scenario it would be unclear which axis to target for slewing, at least initially. Advanced LRF imaging algorithms that use the WFOV camera payload in real-time[5] implement directional slewing once a minimum point cloud density is reached.

Inclination test. The earlier inclination tests are repeated, but this time the orbital path is changed mid-surveillance to induce a different perspective of the RSO. The chaser spacecraft orbits RSO-A for 43 hours at an inclination of 85°, shifts inclination by a varying number of degrees for a final inclination between 76° and 94° and continues surveillance for another 43 hours. Figure 18 shows the results – recall that the lower the score value, the better the reconstruction.

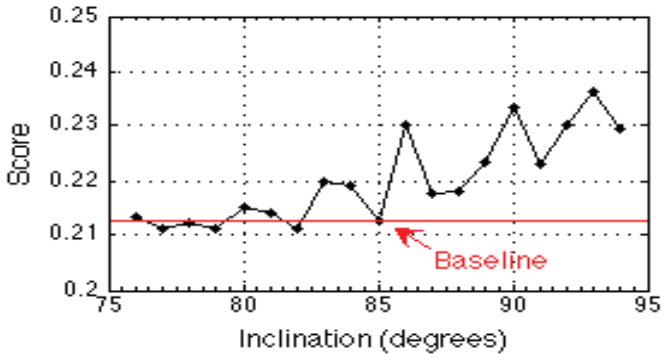

Figure 18: Effect of shifting to a new inclination on RSO-A reconstruction score

It is found that if the spacecraft is already at an inclination that provides good coverage, changing the inclination provides no significant improvement and often produces slightly worse results. Operationally, changing relative inclination can be fuel-intensive, so multiple inclination changes are infeasible; attitude maneuvers are a much more effective way to maximize coverage.

Analysis: LRF's ability to recreate RSO's shape

Recall that it took roughly 172 hours (7.17 days) of the LRF in orbit around the asteroid for the LRF score to approach the LIDAR score. The LIDAR, in turn, took 21.5 hours of asteroid surveillance to achieve that score.

For the RSO case, it is found that it takes more time for the LRF point clouds to approach the LIDAR score. As noted above, this is due in part to the edge metric's interpretation of edge points on solar panels. Figure 19 shows that the LIDAR point cloud is dense enough that few points on the solar panel surface are falsely marked as edge points. However, as seen in Figure 17, due to insufficient density to calculate unique results, the LRF point clouds contain several falsely marked edge points. In addition, the difference in scores indicates loss of fine detail information on the protruding objects on the RSOs.

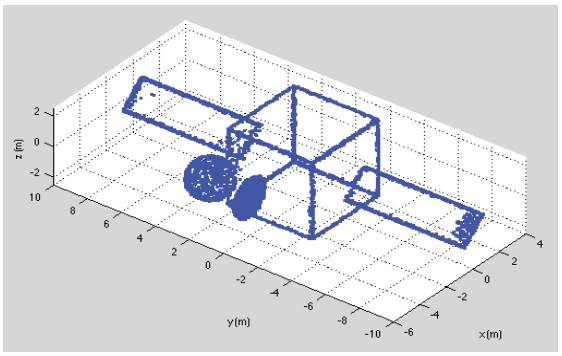

Figure 19: LIDAR coverage of RSO-A: Blue points are detected edges.

It is evident from the figures, however, that the LRF point clouds can approach the level of shape recovery exhibited by the LIDAR in operationally sufficient time, given knowledge of the RSO's attitude motion. From the analysis above it can be concluded that, for error-free measurements, the LRF can effectively create sufficiently dense point clouds for various asteroid and satellite shaped RSOs, with minimal fuel consumption, by exploiting a designed combination of Keplerian and attitude motion.

ERROR MODELS

This section presents the validation of the techniques detailed above through inclusion of two sensor error models. The first is a simple stochastic model that accounts for electrical and environmental noise present in the measurement process, implemented as a normal distribution with a given standard deviation. This Gaussian noise is added directly to the results. The second model takes into account the dilation of the transmitted laser pulse after reflection from a surface exhibiting a slope with respect to the transmitter's optical axis, implemented as a linear function of the slope. With this model, the Gaussian noise added is proportional to the angle between the axis of the beam and the normal of the stricken surface. Stochastic and pulse dilation errors are summed directly to account for the worst case combination of errors. Details of these models are summarized below.

Stochastic Error Model

The stochastic error model for the scanning LIDAR adds Gaussian noise directly to the ideal LIDAR results, to simulate processes that cannot be modeled in details such as timing circuitry

errors. The 3σ values for the azimuth and elevation error add an angular error to each individual LIDAR strike, while the 3σ distance adds an error along the pointing direction. This error model can be directly integrated with COTS LIDAR company specifications. A model based on a Jenoptik scanning LIDAR[3] is used. The specifications and errors of which are found in Appendix A. Figure 20 shows a grid of 5×5 points with measurement error included in the results. The red X's denote the ideal results for comparison.

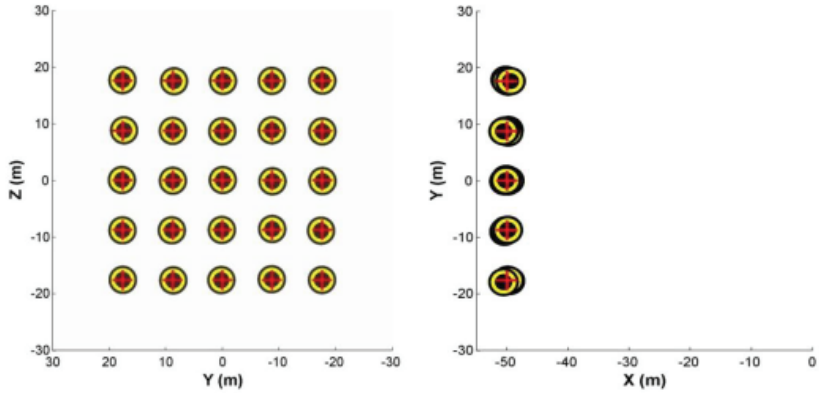

(a) Side View (Y-Z Plane) (b) Top View (X-Z Plane)

Figure 20: LIDAR measurement model with errors typical of the Jenoptik LIDAR.

Figure 21 shows the elevation angle error results for 1000 runs with a 3σ value of 0.2°. The Gaussian-like curve verifies the implementation of the error models. Similar plots are generated for azimuth error angle and the distance error.

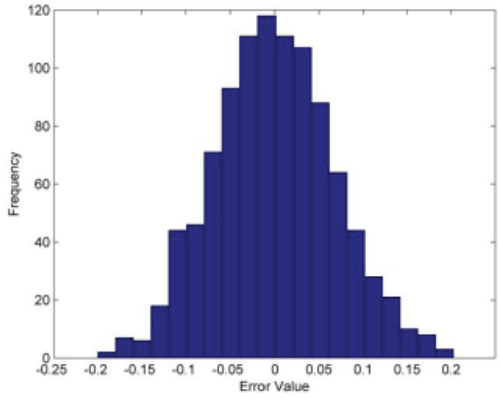

Figure 21: Histogram of 1000 runs of the elevation angle error. The 3σ error is set to 0.2°.

Pulse Dilation Error Model

In reality, an imaging LRF's beam is not a distinct point; it has some beam spread, as illustrated in Figure 22(a). The dotted black line shows the pointing axis of a single-beam LRF.

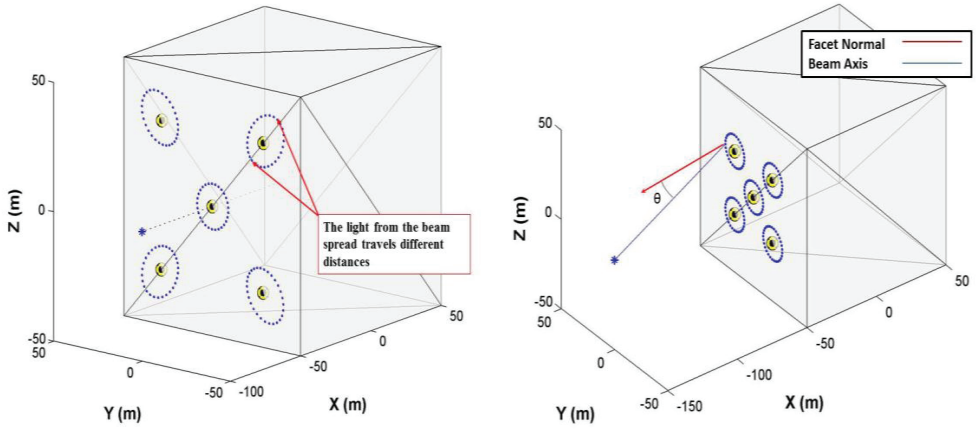

(a) LRF beam spread (b) Angle used to generate pulse dilation error

Figure 22: LRF beam spread and angle illustration. The blue star indicates LRF position.

In order to better model the LRF error resulting from this beam spread, the pulse dilation error model is used. This model adds a Gaussian error to the x, y, and z components of the LRF strike. This error is proportional to the angle θ between the optical axis and a 30-point beam spread, illustrated in Figure 22(b). This angle is calculated for each of these beam spread strikes and averaged together into one error for each LRF or LIDAR "strike". The absolute value of the angle is taken to make this angle always positive. The error function is expressed as the tangent value of θ, seen in Equation (1). This is chosen to simulate that as the angle θ approaches 90^o (or the facet becomes parallel to the beam), the error approaches infinity.

$$err = \frac{\alpha \sum_{i=1}^{m} \tan \theta_i}{3m} \times w \tag{1}$$

In Equation (1), the user-defined parameter α is the 3σ value of the Gaussian error. w is the normally distributed probability function, and m is the number of simulated strikes in the beam spread.

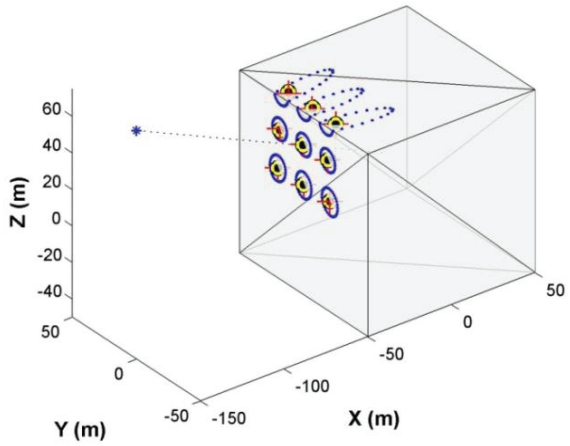

Figure 23: Pulse dilation error model results: No-error results are plotted as red *X*'s.

This is calculated with three different random numbers and added directly to the x, y, and z component of the strike. Finally, a user defined beam spread angle is specified, which is the cone half angle of the beam spread. The pulse dilation error is added only for strikes which directly hit a surface. If the main beam does not hit the surface no output is generated, even if some of the beam spread strikes the target. Figure 23 shows a situation where the beam spread wraps around the surface, for a beam spread cone half angle of 3°.

RESULTS USING ERROR MODELS

Three error scenarios are run for each of the two configurations (i.e. cross and zigzag) and for each of the two models (i.e. ellipsoid and RSO). The first scenario models a Jenoptik scanning LIDAR with errors as specified in Table 1 (i.e. azimuth and elevation angular 3σ errors of $\pm 0.2^{o}$ and 3σ distance errors of ±1m). The second scenario models a configuration of fixed, well characterized LRFs, i.e., no angular error and only a 0.3m 3σ distance error. The range measurement errors are typical of the maximum range of each instrument, i.e., 5km for the scanning LIDAR and 3km for the LRF. The results can be directly extrapolated to the single-beam LRF case. In these two scenarios, only the stochastic error model is used. The last scenario uses a pulse dilation error model shown in Equation 1. The value chosen for α is 0.0002 so that the 3σ error added to each x, y, and z component is less than 1m. The cone half angle of the beam spread is 0.6mrad. Only the pulse dilation error model is considered for the test..

Ellipsoid Imaging

Ellipsoid mapping scenarios are run with identical simulation conditions to the no-error cases (i.e. same field of views, length of time run and time step). A relative radius error is simulated as a ±2m 3σ error in the origin. Considering the application to the ARAPAIMA mission, the focus of the analysis is on the RSO imaging. Table 1 presents the metric scores for ellipsoid mapping contrasted against the ideal measurements case. As expected, inclusion of the error models increases the score.

Table 1. Results for ellipsoid imaging with error models included in the process.

	Error Scenario		No Error
Configuration	**Multi-Beam LRF**	**Pulse Dilation**	
LIDAR	0.2984	N/A	0.0200
Cross LRF	0.1457	0.1503	0.0789
Zigzag LRF	0.1445	0.1428	0.0833

RSO Imaging

RSO Mapping scenarios are run with identical simulation conditions to the no-error cases described previously. The models of the LIDAR and multi-beam LRF, that include stochastic errors and pulse dilation errors, are used in simulations to understand their effects. Results of the multi-beam LRF analysis are easily extended to the single-beam LRF case; errors remain at the same magnitude with longer periods of surveillance around the RSO needed. For brevity these results are not replicated.

Figures 24-26 present the results of satellite-shaped RSO imaging for the same three cases explored with the ellipsoid RSO. Table 2 summarizes the results.

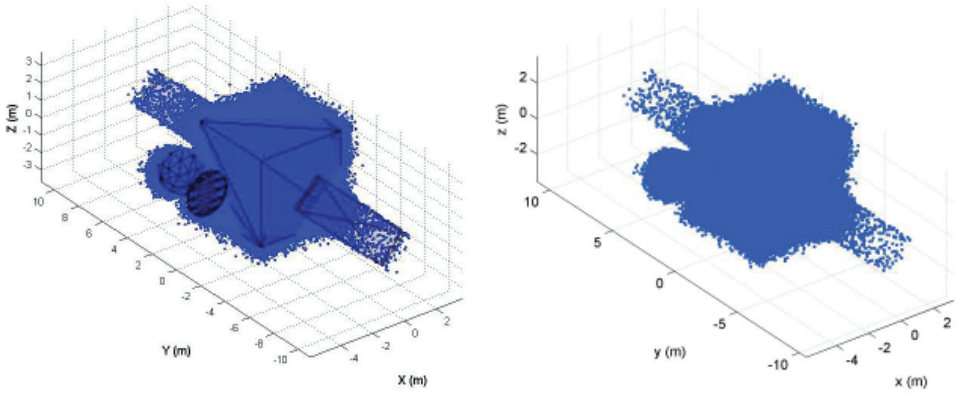

a. Generated Point Cloud b. Edge Detected Points

Figure 24: Results for the scanning LIDAR with stochastic errors in beam elevation, azimuth, and range measurements.

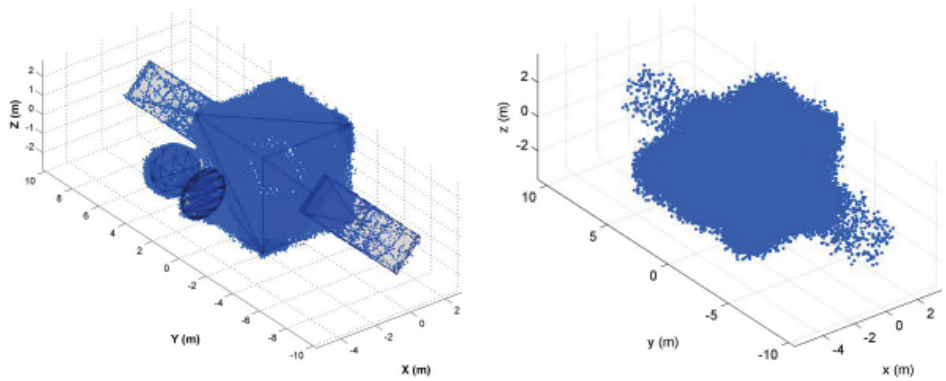

a. Generated Point Cloud b. Edge Detected Points

Figure 25: Results for RSO imaging with the multi-beam LRF in the cross-configuration with stochastic errors in range measurements.

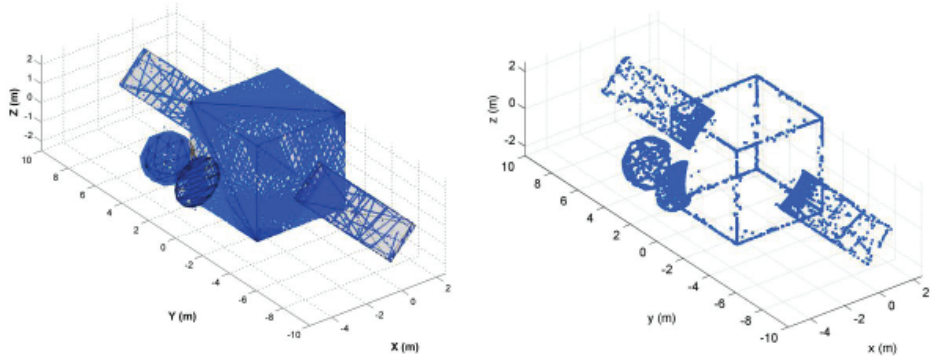

a. Generated Point Cloud b. Edge Detected Points

Figure 26: Results for RSO imaging with the multi-beam LRF in the cross-configurations with pulse dilation errors.

Table 2: Results for RSO imaging with error models included in the process.

	Error Scenario		No Error
Configuration	**Multi-Beam LRF**	**Pulse Dilation**	
LIDAR	0.2984	N/A	0.1100
Cross LRF	0.2457	0.2098	0.1576
Zigzag LRF	0.2415	0.2272	0.1980

CONCLUSIONS

With the error models included in the process, the edge reconstruction of the RSO is problematic. The general shape of the RSO can still be recognized with the naked eye. However, the edge detection algorithm has a hard time detecting the true edges in the point cloud. As seen in Figs. 24-25, the edge recognition algorithm falters on point clouds generated with error models due to the

way it evaluates edge points. If, by removing a point from its neighborhood, the surface variance of the neighborhood is lowered by some threshold, that point is marked as an edge point. However, if the point cloud is noisy, surface variance will decrease when most points are removed from their neighborhoods, resulting in a large number of falsely marked edge points if the threshold is too strict or no edge points at all if the threshold is too generous. The edge metric was not designed to evaluate point clouds with errors and was intended for preliminary investigation into the quality of point clouds in an error-free scenario. *It is important to recognize here that the poor performance of the edge metric on a noisy point cloud is not indicative of point cloud quality or usability*. There are well-tested algorithms such as least squares plane fitting [10] and Voronoi-based reconstruction [11] that have been successfully used to reconstruct surfaces from noisy, non-uniform point clouds such as the ones seen here. While we are unable to effectively compare non-noisy to noisy point clouds using the current metric, the noisy point clouds are still usable for the purposes of 3D surface reconstruction. Exploring the effectiveness of these reconstruction algorithms is a source of future work.

The characterization of the LRF errors is of paramount importance to gain confidence in the simulation process and prescribe performance requirements. Another publication by the authors[9] presents complementary work on characterization of a miniature LRF for space object imaging. Another important aspect of mission design is the specification of pointing knowledge and control requirements that couple with the LRF measurement errors but have not been considered here.

The study concludes that, for error-free measurements, the LRF can effectively create sufficiently dense point clouds for various asteroid and satellite shaped SOs, with low propellant consumption, by exploiting a designed combination of Keplerian and attitude motion. Stochastic and pulse dilation errors are included directly to account for the worst case combination of errors with encouraging results. In addition, a WFOV IR camera is planned as part of the payload for ARAPAIMA, and active imaging with the LRF will supplement passive imaging with the WFOV camera.

Future extensions of the methods presented here, to the design of realistic relative orbits, implementation of closed loop attitude control to close coverage gaps, error modeling for the influence of optical properties of incident materials on LRF accuracy and other SSA applications of this study, are currently in work under the umbrella of the ARAPAIMA program.

ACKNOWLEDGMENTS

This work was performed as a risk reduction exercise for the ARAPAIMA program, funded by the Air Force Office of Scientific Research (AFOSR) and administered by the Air Force Research Laboratory (AFRL) under the University Nanosat Program (UNP).

APPENDIX: JENOPTIK SCANNING LIDAR SPECIFICATIONS

Table 3. Jenoptix Scanning LIDAR specifications[3].

Parameter	Requirement
Field of View (FOV)	≥ 20◦ x 20◦
Frame Rate in Track Mode	≥ 1 Hz
Acquisition Duration	≤ 1 min
Min Operational Range	≤1 m
Max Operational Range	≥ 5000 m
Measurement Accuracy 3σ	R = 5000 m ±1 m R = 1m ± 2 cm
Angular Measurement Accuracy 3σ	≤ 0.2◦
Sensor Mass	10 kg
Power Consumption	50 W

REFERENCES

1 Anthony W. Yu, et. al. "Sixteen Channel, Non-Scanning Airborne LIDAR surface Topography (LIST) Simulator." IEEE 978-1-4577-1005-6, 2011.

2 Anthony W. Yu, et al. "Spaceborne laser instruments for high-resolution mapping." SPIE Vol. 7578 757802-2.

3 Moebius, B., et al. "Imaging LIDAR Technology - Development of a 3D-LIDAR Elegant Breadboard for Rendezvous and Docking, Test Results, and Prospect to Future Sensor Application." International Conference on Space Optics, 2010 October 4 - 8.

4 Nayak, M. V., J. Beck, B. Udrea., "Design of Relative Motion and Attitude Profiles for Three-Dimensional Resident Space Object Imaging with a Laser Rangefinder, " Accepted to the 34th IEEE Aerospace Conference. Big Sky, MT, Mar 2013.

5 Nayak, M. V., J. Beck, B. Udrea., "Closed-loop Attitude Control for Generation of High Density Point Clouds of Resident Space Objects." Accepted to the 34th IEEE Aerospace Conference. Big Sky, MT, Mar 2013.

6 Near Earth Asteroid Rendezvous. Webpage. http://near.jhuapl.edu/sci-eng.html. Accessed 5 Feb 2013.

7 XSS-11 Microsatellite Fact Sheet. Webpage. http://www.kirtland.af.mil/shared/media/document/AFD-070404-108.pdf. Accessed 5 Feb 2013.

8 Le, Binh Q.,T.D. Cole, D.E. Rodriguez, R.A. Reiter, R. C. Moore, M.T. Boies, E.D. Schaefer, L. Stillman, S. Krein. "NEAR Laser Rangefinder Light-weight Packaging Design."Proc. SPIE Vol. 2811, p. 208-216, Photonics for Space Environments IV, Edward W. Taylor; Ed., Oct. 1996.

9 Harris, K., A. Baba, T. Grande, C. Castillo, J. DiGregorio, T. Zuercher, B. Udrea and M. Nayak, "Experimental Characterization of a Miniature Laser Rangefinder for Resident Space Object Imaging." 23rd AAS/AIAA Spaceflight Mechanics Conference, Kauai, HI, Feb 2013.

10 Biggers, K., Wells, C., and Williams, G. "Breaking the Fog: Defining and Orienting Surfaces in Complex Point Cloud Datasets." Technical Report TAMU-CS-TR-2009-4-1, Department of Computer Science, Texas A&M University, College Station, TX, 2009.

11 P. Alliez, D. Cohen-Steiner, Y. Tong, M. Desbrun. "Voronoi-based Variational Reconstruction of Unoriented Point Sets." Proc. Eurographics Symposium on Geometry Processing, 2007, pp. 39-48.